Automated High-Throughput Light-Sheet Fluorescence Microscopy of Larval Zebrafish

Savannah L. Logan[†], Christopher Dudley[†], Ryan P. Baker[†], Michael J. Taormina, Edouard A. Hay, Raghuveer Parthasarathy*

Materials Science Institute , Institute of Molecular Biology, and Department of Physics, The University of Oregon, Eugene, OR 97403

[†] Equal contributors

* Corresponding author: raghu@uoregon.edu

ABSTRACT

Light sheet fluorescence microscopy enables fast, minimally phototoxic, three-dimensional imaging of live specimens, but is currently limited by low throughput and tedious sample preparation. Here, we describe an automated high-throughput light sheet fluorescence microscope in which specimens are positioned by and imaged within a fluidic system integrated with the sheet excitation and detection optics. We demonstrate the ability of the instrument to rapidly examine live specimens with minimal manual intervention by imaging fluorescent neutrophils over a nearly 0.3 mm^3 volume in dozens of larval zebrafish. In addition to revealing considerable inter-individual variability in neutrophil number, known previously from labor-intensive methods, three-dimensional imaging allows assessment of the correlation between the bulk measure of total cellular fluorescence and the spatially resolved measure of actual neutrophil number per animal. We suggest that our simple experimental design should considerably expand the scope and impact of light sheet imaging in the life sciences.

INTRODUCTION

Light sheet fluorescence microscopy (LSFM) is a powerful tool for examining the three-dimensional structural and temporal dynamics of living systems. In LSFM, a thin sheet of laser light excites fluorophores in a sample. Scanning the sample through the sheet enables fast, three-dimensional imaging with low phototoxicity, high resolution, and a wide field of view (1–5). Imaging with LSFM has enabled numerous studies of embryonic development (6,7), neural activity (8), microbial dynamics (9–11), and other phenomena. A large body of work has focused on improving the optical capabilities of light sheet imaging, for example using structured illumination (12,13), multiple lens pairs (6), two-photon excitation (14), and

other techniques. However, current light sheet fluorescence microscopes have significant constraints related to throughput and sample handling that, we argue, have placed much greater limitations on their scientific utility than issues of spatial or temporal resolution. The majority of existing light sheet fluorescence microscopes, both commercial and non-commercial, are designed to hold a single specimen. A few instruments (including one from the authors of this paper) can hold up to six specimens for sequential imaging. Moreover, light sheet fluorescence microscopy typically requires extensive sample preparation and manual sample mounting, most commonly by embedding specimens in agarose gels. Examination of large numbers of specimens is therefore slow and difficult, which is especially important given the high level of inter-individual variability found in many complex biological processes. Increasing the pace of insights into developmental biology, multicellular biophysics, or microbial community structure will require faster and simpler acquisition of three-dimensional imaging datasets. To date, there exists only one report of an automated light sheet microscope that makes use of fluidic positioning of live animals (15); its throughput (specimens per hour) is not stated, and though its ability to image larval zebrafish is clear, the total number of animals examined was only twelve. In contrast, automated, high-throughput methods have been integrated with other types of microscopes, including confocal microscopes (16–18), about which we comment further in the Discussion. Our system adopts and builds upon these, especially the confocal-based setup of Ref. (16).

To address the issues described above, we developed a light sheet fluorescence microscope capable of automated, high-throughput imaging of live specimens. Our instrument uses fluidic control and image-based registration to rapidly but precisely position specimens for light sheet scans and subsequently remove them from the imaging area. We

61 characterize the optical quality of our instrument, and demonstrate its capabilities by rapidly
62 imaging immune cells in dozens of larval zebrafish. While the spatial resolution of our
63 microscope does not equal that of current "low-throughput" light sheet microscopes, it is
64 more than sufficient for determining cellular distributions. Moreover, we argue that the
65 tradeoff of lower resolution for higher throughput is worthwhile given the large variance in
66 most biological datasets.

67 We illustrate the utility of the instrument by imaging neutrophils in dozens of larval
68 zebrafish. Neutrophils are an important and highly dynamic cell type of the innate immune
69 system. These cells migrate to sites of damage or infection and recognize and kill pathogenic
70 microbes (19). Zebrafish are a well recognized model organism for studying neutrophil
71 responses (20,21), and prior work has uncovered changes in neutrophil distributions in
72 response to wound-induced chemotaxis (22), drugs that lead to symptoms similar to human
73 enterocolitis (23), and stimulation by gut microbes or bacterial lipopolysaccharide (LPS)
74 (24,25), to list a few of many examples. Quantifing even basic properties such as neutrophil
75 abundances over large extents for the dozens of specimens required given the high variance
76 between individuals often necessitates slow confocal imaging or painstaking histological
77 sectioning or gut dissection (24–26). These sorts of studies will be greatly facilitated by
78 instruments that can provide large-scale 3D imaging of automatically detected and imaged
79 specimens.

80 We show, as expected, a high degree of variation between fish in total neutrophil
81 number and an increase in its mean value following LPS exposure, as well as spatial
82 clustering of neutrophils in two distinct regions near the swim bladder. While our instrument
83 is optimized for imaging of larval zebrafish, the design could easily be modified for rapid

84 imaging of a wide range of biological and non-biological samples, which should broaden the
85 impact of light sheet microscopy in a variety of fields.
86

87 ## RESULTS

88 ### Instrument design

89 The light sheet portion of the microscope closely follows the design of Keller et al (1); a
90 rapidly-scanned galvanometer creates a sheet of light for fluorescence excitation, and emitted
91 light is captured by a camera perpendicular to the plane of the sheet (Fig. 1A). In
92 conventional light sheet fluorescence microscopes, gel-mounted specimens are introduced
93 vertically in between horizontal lenses. To achieve high throughput, we use a continuous
94 fluidic path through plastic tubing and glass capillaries for transport as well as imaging,
95 detailed below. If the fluidic path were oriented vertically, specimens would gravitationally
96 drift during imaging. Therefore, we adopted a geometry in which specimens are transported
97 horizontally and the sheet plane is vertical (Fig. 1A,B). To allow this arrangement, we
98 designed an elongated sample chamber with windows oriented below and perpendicular to
99 the sample (Fig. 1B,C). Before entering the imaging chamber, specimens flow through a
100 system of 0.7 mm diameter plastic tubing at a typical flow rate of 1 ml/min, or 4 cm/sec
101 (Fig. 1). Flow speed and direction are controlled by a syringe pump (Fig. 1); see
102 Supplemental Methods for a parts list and descriptions.

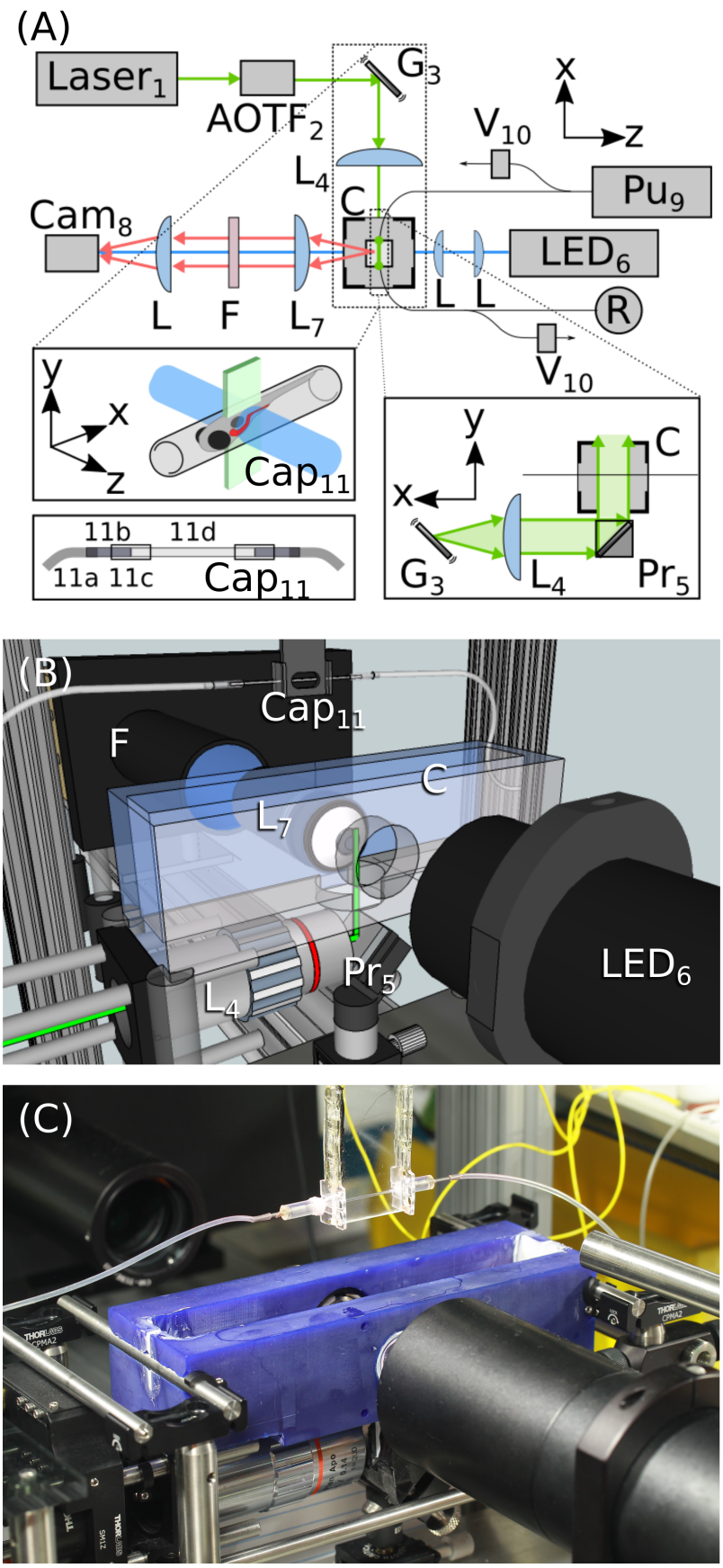
(A)
Laser1
AOTF2
G3
x
z
V10
L4
C
Pu9
Cam8
LED6
L
F
L7
L
L
R
V10
y
x
z
Cap11
11b
11d
11a 11c
Cap11
y
C
x
G3
L4
Pr5
(B)
Cap11
F
C
L7
Pr5
LED6
L4
(C)

103

Figure 1. Instrument design. (A) Schematic of the instrument design, with labels corresponding to the parts list in Table 1. See also Supplementary Movie 1. The excitation laser line is selected by an acousto-optic tunable filter ($AOTF_2$) , then directed to a galvanometer mirror (G_3) and objective lens (L_4) to create a time-averaged sheet of light in the sample chamber (C) via a prism (Pr_5). Specimens flow through a system of tubing controlled by a syringe pump (Pu_9) and valves (V_{10}) and are automatically positioned in a square-walled capillary (Cap_{11}) for imaging. Bright field images are used for positioning the sample and are illuminated with an LED (LED_6). After imaging, specimens are directed into a reservoir (R). **(B)** Schematic of the imaging area. The 3D-printed sample chamber (C), prism (Pr_5), and imaging capillary (Cap_{11}) are apparent. **(C)** Photograph of the imaging area corresponding to the schematic in (B).

Inside the imaging chamber, specimens flow into a square-walled glass capillary in front of the imaging objective where they are automatically detected by bright field microscopy. Specimens are rapidly stopped using computer-controlled valves on either side of the imaging chamber, with a precision of approximately 1 mm in position, comparable to the length of a larval zebrafish. Fine positioning is performed by iterated movement of the capillary by a computer-controlled stage, brightfield imaging, and comparison of images with a previously assembled image library (see Methods) (Fig. 2 A,B). The travel range of the capillary on the stage allows movement of up to 30 mm in the x-direction. Like many studies, ours make use of larval zebrafish as a model organism; strong features such as eyes and the swim bladder enable straightforward correlation-based registration, with a precision

128 of about 20 μm as described below. This approach should be applicable to any specimen
129 with a roughly sterotypical anatomy. The specimen is not rotated about the tube axis; we
130 comment further on this in the Discussion section.
131
132 Once positioned, specimens are automatically imaged using LSFM. The imaging chamber
133 has sufficient depth, 35 mm, that the capillary can be scanned through the sheet by a
134 motorized stage. In our setup, repeated scans with up to three excitation wavelengths are
135 possible; this is limited simply by the number of available laser lines. The precision of the
136 automated positioning enables scans to be taken of particular regions, for example the larval
137 gut, as shown below. After imaging, specimens flow into a collection reservoir and
138 subsequent specimens are automatically positioned for imaging. We provide a movie of the
139 instrument in operation as Supplementary Video S1. A complete parts list is provided as
140 Table 1, in Supplemental Methods.
141
142 **Optical quality**
143 Our instrument uses glass capillaries for specimen mounting, rather than more conventional
144 gel embedding. The square cross-section of these capillaries should lead to less distortion
145 than more common cylindrical capillaries. To assess the optical quality of our setup, we
146 measured the point spread function (PSF) by imaging 28 nm diameter fluorescent
147 microspheres dispersed in oil in these capillaries (see Methods for details). The diffraction-
148 limited width of the particles in the sheet plane (*xy*), assessed as the standard deviation of a
149 Gaussian function fit to the particle's intensity profile, is 0.6 μm, and the width along the
150 detection axis (*z*) is 3.4 ± 0.6 μm, consistent with the expected sheet thickness of our setup
151 (Fig. 2 C,D).

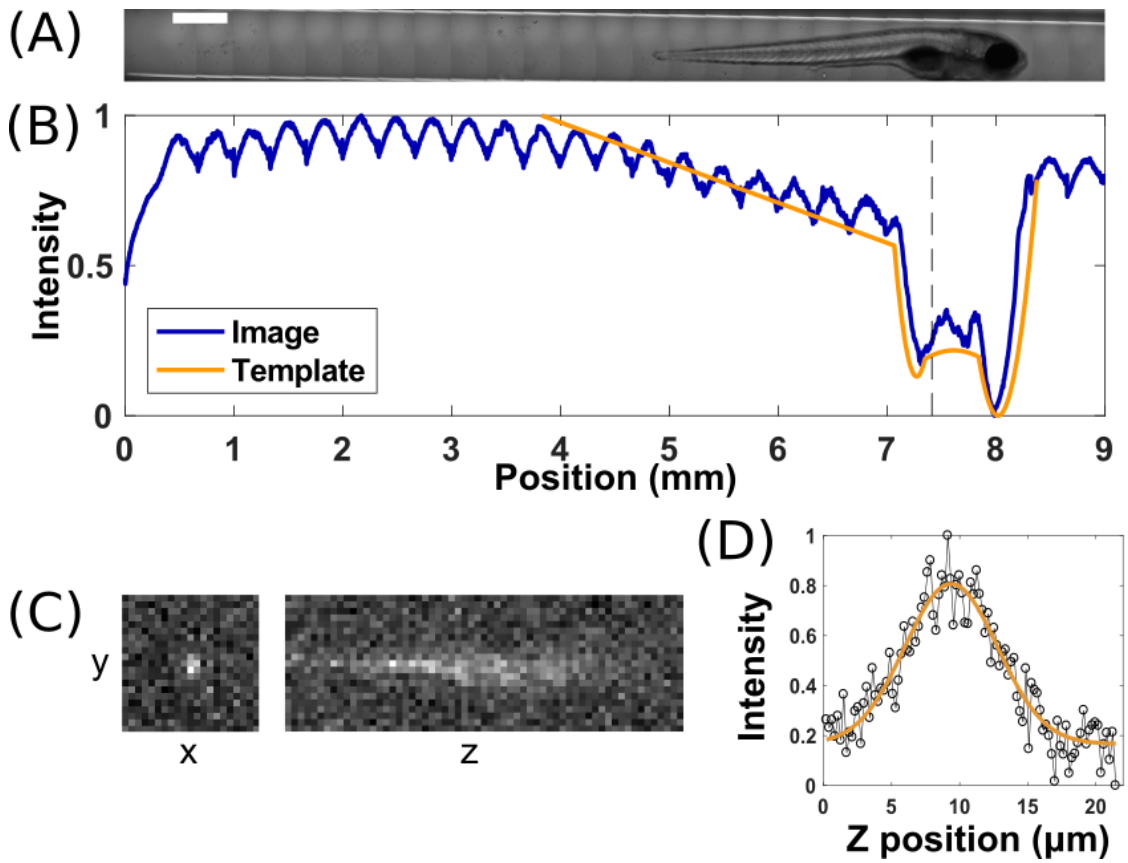

Figure 2. Specimen positioning and image quality. (A) Composite brightfield image of a larval zebrafish positioned in a glass capillary. Scale bar: 50 μm. (B) Normalized intensity averaged along the short axis of the brightfield image, and the intensity of the template image that best matches the fish in (A). Cross-correlation with the template is used to automatically position the fish for light sheet fluorescence imaging. (C) Light sheet fluorescence images of a 28 nm diameter fluorescent microsphere, showing *x-y* and *z-y* planes centered on the particle. (D) Line-scan of intensity along the detection axis (*z*) through a fluorescent microsphere, with a Gaussian fit showing a width of approximately 3 μm.

165 **Data collection capabilities**

166 Using this system, we can image approximately 30 larval zebrafish per hour, obtaining from
167 each a 666 x 431 x 1060 μm (*x, y, z*) three-dimensional scan, a marked improvement over
168 manual mounting and imaging that, even by a skilled researcher, is limited to about 5 fish per
169 hour. The triggering accuracy is about 90%, with roughly 10% of detected objects being
170 bubbles or debris that are easily identified after imaging. On average, 81% of larval fish are
171 automatically positioned correctly in front of the imaging objective. The remaining 19%
172 correspond to multiple fish being in the field of view, or other positioning errors.
173 Importantly, the majority of the run time of the instrument is spent obtaining light sheet
174 fluorescence images, and is not dominated by specimen positioning. In the batch of N=41
175 fish whose neutrophil distributions were imaged in experiments described below, for
176 example, the flow, detection, and positioning of the specimens occupied only approximately
177 30 seconds per fish. In the limit of zero imaging time (e.g. for very bright signals or small
178 regions of interest), the system could therefore record data from up to about 120 specimens
179 per hour in the absence of triggering or positioning errors, or about 90 specimens per hour
180 with the present system performance.

181

182 **Neutrophils in larval zebrafish**

183 To demonstrate the capabilities of the instrument, we imaged fluorescent neutrophils in
184 larval zebrafish at 5 days post-fertilization (dpf), focusing especially on the number of these
185 immune cells and their distribution near the anterior of the intestine. Specifically, these were
186 fish engineered to express green fluorescent protein (GFP) under the promoter
187 myeloperoxidase, an enzyme primarily produced in neutrophils (27).

188

189 **Positioning accuracy**

190 To assess the positioning accuracy of our instrument, we performed automated scans of
191 larval zebrafish with GFP-expressing neutrophils, and then reloaded the same fish and re-
192 scanned them. Changes in the neutrophil positions are due to both imaging error and to
193 motion of the neutrophils during the intermediate time. (Neutrophils are highly motile cells,
194 crawling through tissue and also entering or leaving tissue via the bloodstream.) For five
195 twice-scanned fish, we manually identified three neutrophils that were unambiguously the
196 same in each scan (i.e. not newly entered or departed). For these neutrophils, the within-fish
197 standard deviations of the changes in position provide a measure of the biological variation,
198 e.g. from neutrophil motion. These were 5.3 ± 3.5 μm, 11.6 ± 9.0 μm, and 40.0 ± 36.4 μm,
199 for x, y, and z, respectively, where x is the flow direction and z is perpendicular to the light
200 sheet. The standard deviation between fish of the mean neutrophil positions provides a
201 measure of the instrumental variation, e.g. from imperfect positioning. These were 18.9 ±
202 6.7 μm, 56.1 ± 19.9 μm, and 52.6 ± 18.6 μm for x, y, and z, respectively. Along the capillary
203 axis, therefore, the fish positioning is reproducible to within about 20 μm. The larger
204 variance in y and z is expected, as we are not explicitly detecting location along these axes,
205 and because there can be specimen rotation about the x-axis. Overall, therefore, global
206 positioning uncertainty is on the order of a cell diameter for cells such as neutrophils.

207

208 **Neutrophil number and variance**

209 In total, we imaged 41 fish, obtaining from each a single 666 x 431 x 1060 μm three-
210 dimensional image in which neutrophils were readily evident (Fig. 3A and Supplementary
211 Movie S2). Brightfield images are captured and saved prior to fluorescence imaging; a set of
212 four such images, demonstrating their appearance and variance, are provided as

213 Supplemental Figure 1. The strong GFP signal enabled automated identification of
214 neutrophils by standard segmentation methods. Corroborating previous work done by
215 manual dissection of zebrafish (24), we found a high degree of variation in neutrophil
216 number between specimens, with the standard deviation being 30% of the mean (Fig. 3B).
217 Furthermore, we found that neutrophils tend to cluster in two distinct regions: adjacent to
218 the swim bladder on both the anterior and posterior (Fig. 3C). Notably, the total GFP
219 intensity in a fish is weakly correlated with the number of neutrophils, with a coefficient of
220 determination $R^2 = 0.4$, indicating that a simple measure of overall brightness, as could be
221 assessed without three-dimensional microscopy, would provide a poor diagnostic of the
222 actual abundance of immune cells (Fig. 3D). We also compared neutrophil counts
223 determined from two-dimensional maximum intensity projections of the full three-
224 dimensional image stacks, mimicking images that would be obtained from simple widefield
225 fluorescence microscopy. This yielded a number of neutrophils that was on average $0.76 \pm$
226 0.02 of that from the three-dimensional counts, indicating as expected that some neutrophils
227 are behind others in the three-dimensional space of the specimen, and hence require three-
228 dimensional imaging for accurate assessment (Supplemental Figure 2).

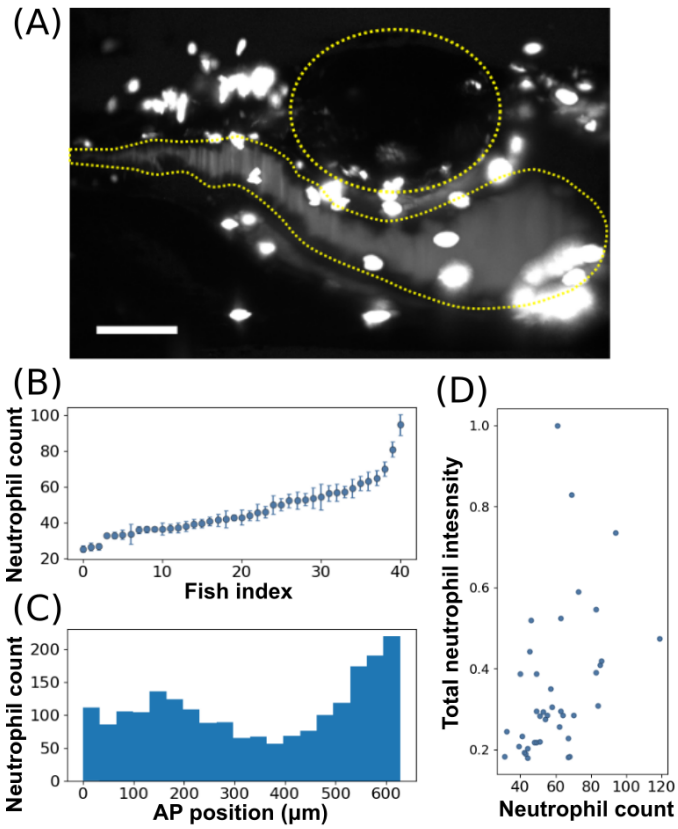

Figure 3. Imaging neutrophils in larval zebrafish. (A) A maximum intensity projection of a three-dimensional light sheet fluorescence image of GFP-expressing neutrophils near the intestine of a 5 dpf larval zebrafish. The 3D scan is provided as Supplemental Movie 2. The intestine and swim bladder are roughly outlined by the yellow dotted lines. Scale bar: 100 μm. (B) The total number of neutrophils in each fish; the x-axis is ordered by neutrophil count. (C) Neutrophil count along the anterior-posterior dimension, summed over all fish examined (*N*=41). The x-axis corresponds approximately to the horizontal range of (A). (D) The total intensity of the detected neutrohils per fish vs the total number of neutrophils in that fish. The two measures are weakly correlated with a coefficient of determination $R^2 = 0.4$.

242

243 In addition, we examined neutrophil number in response to exposure of larval
244 zebrafish to soluble LPS, the major component of the outer membrane of gram negative
245 bacteria, known from earlier studies to stimulate an inflammatory immune reaction (25,28).
246 As above, we detected and scanned transgenic zebrafish with GFP-expressing neutrophils,
247 exposed to LPS in their flask water at a concentration of 150 μg/ml for 0 (control), 2, and 24
248 hours prior to imaging. As above, neutrophil number shows a large degree of variability. At 5
249 dpf, we detected 85.0 ± 17.0 (N = 13) and 87.6 ± 27.6 (N = 14) (mean ± standard
250 deviation) neutrophils in fish subjected to no LPS and LPS for 2 hours, respectively;
251 indicating no discernible change. At 6 dpf, we detected 95.1 ± 23.4 (N = 21) and 114.2 ±
252 38.1 (N = 19) in the control and 24-hour LPS-treated fish, respectively, indicating an
253 increase in the mean neutrophil count by a factor of 1.2 ± 0.1.

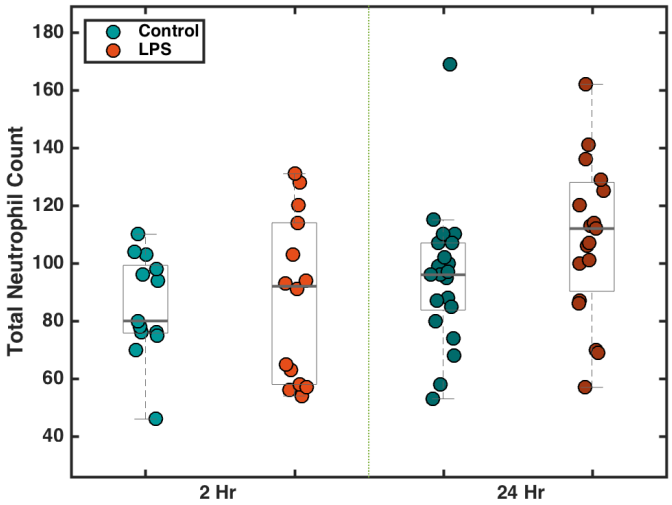

254

255 **Figure 4. Neutrophil counts after exposure to LPS.** The number of
256 neutrophils counted from light sheet fluorescence images of larval zebrafish
257 after exposure to 150 μg/ml LPS for 0 (control), 2, or 24 hours. At 2 hours

post-exposure, there was no discernible difference between the LPS-treated group and the control group. At 24 hours post-exposure, the LPS group displayed an increase in mean neutrophil count of 1.2 ± 0.1.

DISCUSSION

In recent years, many instruments for high content and high throughput imaging of small organisms, such as embryonic and larval zebrafish, have been developed (15–18,29–32), and have demonstrated their utility for fast, accurate imaging and screening. Our setup has similarities and differences to several of these, and advantages and disadvantages for particular applications. Several instruments are designed to image specimens held in multi-well plates (29–32), including commercial instruments such as the ImageXpress High-Content Screening System (33) and the Acquifer Imaging Machine (34). These plate-based systems enable integration with standard specimen containment, and also facilitate automated delivery of chemicals or other perturbations. Imaging is typically provided by widefield microscopy, which is rapid and simple but which prohibits three-dimensional imaging. While confocal microscopy is in principle possible, the thickness of standard plate bottoms would make this difficult except for specialized setups. Three-dimensional confocal fluorescence microscopy is, however, attained in automated instruments such as those of Refs. (16) and the commercial VAST device (35), which use capillary- and tubing-based automated specimen handling and positioning. While successful, and enabling a wide range of studies, there are applications for which the advantages of light sheet microscopy compared to confocal microscopy, namely its rapid speed and low phototoxicity (1–5,36), are important, such as the imaging of active cells in dynamic environments like the intestine. The requirement of orthogonal accessible light paths for light sheet imaging make its

282 integration with existing high-throughput instruments non-trivial, motivating the work
283 presented here. Our design of a relatively freestanding capillary amid a vertical excitation
284 sheet and horizontal detection axis is effective, but it need not be the only solution. For
285 example, one could imagine integration with single-lens-based light sheet techniques (37,38),
286 and it will be interesting to see if such schemes are developed. We note that our device will
287 have lower throughput than plate-based instruments, and will not integrate with commercial
288 confocal microscopes as existing tubing-based methods do, but rather will enhance studies
289 for which light sheet fluorescence microscopy allows insights into dynamic biological
290 phenomena that are otherwise unattainable.

291 While our microscope is optimized for rapid imaging of larval zebrafish, the design is
292 general and opens numerous possibilities for imaging a wide range of specimens, such as
293 organoids, drosophilia embryos, small marine invertebrates, and more, with the appropriate
294 expansion of the positioning image library.

295 Our design does not rotate the specimen about the travel axis, a design choice that
296 has advantages and disadvantages for applications. It is certainly possible to vary the
297 specimen orientation by rotating the glass capillary, as, for example, in the VAST instrument
298 (35). Rotation would enhance image quality, both by allowing the selection of particular
299 orientations with minimal sheet distortion and by enabling the fusion of multiple views to
300 gain isotropic resolution. We note, moreover, that variation in image quality due to the
301 uncontrolled orientations of zebrafish likely contributes, along with true biological variability,
302 to the total scatter in neutrophil counts (Figs. 3, 4). The ability to examine a large number of
303 specimens allows averaging over both sources of variation. Though it could be implemented,
304 rotational positioning of each animal takes time and, at least in our design, significantly
305 reduces the throughput of the instrument. Furthermore, we believe that many useful

306 applications, e.g. the neutrophil counting demonstrated here, can be realized without
307 specimen rotation, and that the simplicity of the setup as presented can hopefully foster
308 widespread adoption. We note that rotation can be decoupled from the imaging area, as in
309 Ref. (35), so that one specimen can be oriented while another is imaged, preventing a
310 reduction in throughput. Such additions to the instrument described, though carrying a cost
311 of greater complexity, may be worthwhile.

312 While the present design provides only a single three-dimensional image of each
313 specimen, we envision future integration of a closed-loop fluidic circuit, with which
314 specimens can be automatically loaded, imaged, and circulated repeatedly, allowing for high-
315 throughput acquisition of multiple snapshots of the same specimen over time. In general,
316 tackling the challenge of automated, high-throughput specimen handling will allow the
317 technique of light sheet fluorescence microscopy to maximize its impact on the life sciences.
318

319 ## METHODS

320 ### Hardware

321 The majority of the instrument was constructed with off the shelf parts. Custom parts were
322 either laser cut from acrylic sheets or were 3D printed (see Parts List).
323

324 Fluorescence excitation is provided by various solid state lasers, selected by an acousto-optic
325 tunable filter (AOTF, AA Opto-electronic) for coupling into a fiber launch to a
326 galvanometer mirror (Cambridge Technology), which oscillates with a triangular waveform
327 at 1 kHz to sweep the beam into a sheet. An objective lens (Mitutoyo 5X) and a prism route
328 the sheet to the water-filled sample chamber where it intersects the specimen (Fig. 1).
329 Detection is provided by a 20x water immersion objective (Olympus 20XW), mounted in the

330 side of the chamber and sealed with an o-ring, its corresponding tube lens, and an sCMOS
331 camera (Hamamatsu Orca Flash 4.0). Exposure times were 25 ms for all experiments
332 presented here. Instrument control software was written in MATLAB.
333
334 **Ethics statement**
335 All zebrafish experiments were carried out in accordance with protocols approved by the
336 University of Oregon Institutional Animal Care and Use Committee (39).
337
338 **Zebrafish husbandry**
339 The zebrafish line *Tg[BACmpo:gfp]* (27) was used for neutrophil imaging. Larval zebrafish
340 were raised at a density of one embryo per milliliter and kept at a constant temperature of 28
341 ^{o}C. Embryos were not fed during experiments and were sustained by their yolks.
342
343 **Sample preparation**
344 Larval zebrafish were placed in dishes containing sterile embryo media with 0.05%
345 methylcellulose and anaesthetized using 240 μg/ml tricaine methanesulfonate. This
346 anaesthetic concentration is higher than the standard dosage, but was necessary likely
347 because of permeation through the plastic tubing. Specimens are initially loaded into the
348 tubing system by manual aspiration using a syringe connected to the opposite end of the
349 tubing, maintaining a spacing between specimens of approximately 6 inches. Fish are pulled
350 into the tubing head-first to ensure high and consistent flow speeds. (Fish travel better
351 forwards than backwards). During experiments, larvae flowed through the tubing and were
352 automatically stopped and positioned by a syringe pump and a series of valves. After
353 imaging, larvae flowed into a dish containing sterile embryo medium.

354

355 **LPS Treatment**

356 A filter-sterilized LPS (*E. coli* serotype 0111:B4, Sigma) solution was injected into flasks
357 containing 15 zebrafish larvae at 5 dpf for a final concetration of 150 μg/ml of LPS in each
358 flask. Fish were incubated in the LPS solution for 2-24 hours as indicated in the text, after
359 which they were removed from the solution and imaged.

360

361 **Imaging Procedure**

362 For live imaging, each larval zebrafish flows through 0.7 mm inner diameter silicone tubing
363 to a 50 mm long section of round 0.7 mm inner diameter, square exterior cross section, glass
364 tubing in the specimen chamber. The contrast between the specimen and background in
365 brightfield images is used to detect the specimen, stop the pump, and close off tubing using
366 pinch valves to prevent specimen drift. Detecting the specimen and halting the flow places
367 the specimen within three to five millimeters of the desired location. Fine positioning of the
368 specimen is performed by translating the specimen along the capillary axis ("x") in roughly
369 30 steps of 0.3 mm size, capturing a brightfield image at each position, tiling the brightfield
370 images into one large image, and comparing the result with a previously assembled "library"
371 image. The comparison can be done in one of two ways, which yield indistinguishable
372 positioning accuracies, both of which begin by averaging the image intensity along the "y"
373 direction, giving a one-dimensional intensity profile. The profile is then compared with the
374 profile derived from average library images either (i) by cross-correlation, in which one
375 profile is offset in position and then multiplied by the other profile, and integrated
376 (summed), giving a correlation value as a function of offset value, or (ii) the location of the
377 profile's intensity minimum is determined, and compared to the location of the average

378 library profile's minimum. In (i) the peak in the correlation function and in (ii) the difference
379 between the minima gives the displacement between the profile and the library profile, and
380 therefore indicates where the specimen should be precisely positioned. Following
381 positioning, bright field illumination is switched off and the desired laser wavelength is
382 selected by the AOTF. The *xyz* arm is then scanned perpendicular to the sheet plane,
383 generating a 3D image stack. The scan can be repeated for another region or another
384 wavelength before the pump is directed to send the specimen out of the chamber, and bring
385 in the next specimen.
386
387 **Point Spread Function**
388 For measurements of the point spread function, 28 nm diameter fluorescent carboxylate-
389 modified polystyrene spheres (Thermo Fisher cat. #F8787), with peak excitation and
390 emission wavelengths 505 and 515 nm, respectively, were dispersed in oil with a similar
391 index of refraction as water (Zeiss Immersol W 2010) inside the imaging capillaries. Three-
392 dimensional scans were taken, with a z-spacing of 0.5 μm.
393
394 **Image-based neutrophil quantification**
395 Neutrophils were detected from image stacks using custom code written in Python,
396 involving a coarse and fine thresholding. First, the 3D stack was thresholded using a low
397 intensity value followed by the morphological operations of closing and erosion with a range
398 of 1 pixel (40). Connected above-threshold pixels were identified as objects using scikit-
399 image's label function. Then, each detected object was further thresholded using an Otsu
400 filter and labeled again. This re-thresholding process was repeated twice, and objects below 3
401 μm^3 in volume were discarded as unphysical. The total intensity within each identified object

402 represents the total fluorescence intensity of that neutrophil. For a full 3D dataset, the
403 processing takes 1-2 minutes.
404
405 **Raw data**
406 Raw image data, roughly 150 GB in total size, is available from the authors on request.
407

408 ## ACKNOWLEDGEMENTS

409 We thank Rose Sockol, Kyleah Murphy, and the University of Oregon Zebrafish Facility
410 staff for fish husbandry, and Karen Guillemin and Brandon Schlomann for useful comments
411 and conversations. Research reported in this publication was supported in part by the
412 National Science Foundation (NSF) under award 1427957 (to RP), by the the M. J. Murdock
413 Charitable Trust, and by the National Institutes of Health (NIH) as follows: by the National
414 Institute of General Medical Sciences under award number P50GM098911 and by the
415 National Institute of Child Health and Human Development under award P01HD22486,
416 which provided support for the University of Oregon Zebrafish Facility. The content is
417 solely the responsibility of the authors and does not represent the official views of the NIH,
418 NSF, or other funding agencies.
419

420 ## REFERENCES:

421 1. Keller PJ, Schmidt AD, Wittbrodt J, Stelzer EHK. Reconstruction of Zebrafish Early
422 Embryonic Development by Scanned Light Sheet Microscopy. Science. 2008 Nov
423 14;322(5904):1065–9.

424 2. Power RM, Huisken J. A guide to light-sheet fluorescence microscopy for multiscale
425 imaging. Nat Methods. 2017 Apr;14(4):360–73.

426 3. Keller PJ, Ahrens MB, Freeman J. Light-sheet imaging for systems neuroscience
427 [Internet]. Nature Methods. 2014 [cited 2018 Mar 22]. Available from:
428 https://www.nature.com/articles/nmeth.3214

429 4. Huisken J. Slicing embryos gently with laser light sheets. BioEssays [Internet]. 2012
430 [cited 2018 Mar 22];34. Available from:
431 https://www.readcube.com/articles/10.1002/bies.201100120

432 5. Santi PA. Light Sheet Fluorescence Microscopy. J Histochem Cytochem. 2011 Feb
433 1;59(2):129–38.

434 6. Tomer R, Khairy K, Amat F, Keller PJ. Quantitative high-speed imaging of entire
435 developing embryos with simultaneous multiview light-sheet microscopy. Nat
436 Methods. 2012 Jul;9(7):755–63.

437 7. Weber M, Scherf N, Meyer AM, Panáková D, Kohl P, Huisken J. Cell-accurate optical
438 mapping across the entire developing heart. eLife. 2017 Dec 29;6:e28307.

439 8. Keller PJ, Ahrens MB. Visualizing Whole-Brain Activity and Development at the Single-
440 Cell Level Using Light-Sheet Microscopy. Neuron. 2015 Feb;85(3):462–83.

441 9. Wiles TJ, Jemielita M, Baker RP, Schlomann BH, Logan SL, Ganz J, et al. Host Gut
442 Motility Promotes Competitive Exclusion within a Model Intestinal Microbiota. PLOS
443 Biol. 2016 Jul 26;14(7):e1002517.

444 10. Logan SL, Thomas J, Yan J, Baker RP, Shields DS, Xavier JB, et al. The Vibrio cholerae
445 Type VI Secretion System Can Modulate Host Intestinal Mechanics to Displace
446 Commensal Gut Bacteria. bioRxiv. 2017 Nov 29;226472.

447 11. Parthasarathy R. Monitoring microbial communities using light sheet fluorescence
448 microscopy. Curr Opin Microbiol. 2018 Jun;43:31–7.

449 12. Chen B-C, Legant WR, Wang K, Shao L, Milkie DE, Davidson MW, et al. Lattice light-
450 sheet microscopy: Imaging molecules to embryos at high spatiotemporal resolution.
451 Science. 2014 Oct 24;346(6208):1257998.

452 13. Chang B-J, Meza VDP, Stelzer EHK. csiLSFM combines light-sheet fluorescence
453 microscopy and coherent structured illumination for a lateral resolution below 100 nm.
454 Proc Natl Acad Sci. 2017 May 9;114(19):4869–74.

455 14. Truong TV, Supatto W, Koos DS, Choi JM, Fraser SE. Deep and fast live imaging with
456 two-photon scanned light-sheet microscopy. Nat Methods. 2011 Sep;8(9):757–60.

457 15. Gualda EJ, Pereira H, Vale T, Estrada MF, Brito C, Moreno N. SPIM-fluid: open source
458 light-sheet based platform for high-throughput imaging. Biomed Opt Express. 2015
459 Nov 1;6(11):4447–56.

460 16. Pardo-Martin C, Chang T-Y, Koo BK, Gilleland CL, Wasserman SC, Yanik MF. High-
461 throughput *in vivo* vertebrate screening. Nat Methods. 2010 Aug;7(8):634–6.

462 17. Yanik MF, Rohde CB, Pardo-Martin C. Technologies for Micromanipulating, Imaging,
463 and Phenotyping Small Invertebrates and Vertebrates. Annu Rev Biomed Eng.
464 2011;13(1):185–217.

465 18. Hwang H, Lu H. Microfluidic tools for developmental studies of small model organisms
466 — nematodes, fruit flies, and zebrafish. Biotechnol J. 2013 Feb;8(2):192–205.

467 19. Mayadas TN, Cullere X, Lowell CA. The multifaceted functions of neutrophils. Annu
468 Rev Pathol. 2014;9:181–218.

469 20. Meijer AH, Spaink HP. Host-pathogen interactions made transparent with the zebrafish
470 model. Curr Drug Targets. 2011 Jun;12(7):1000–17.

471 21. Galindo-Villegas J. Recent findings on vertebrate developmental immunity using the
472 zebrafish model. Mol Immunol. 2016 Jan 1;69:106–12.

473 22. Kadirkamanathan V, Anderson SR, Billings SA, Zhang X, Holmes GR, Reyes-Aldasoro
474 CC, et al. The Neutrophil's Eye-View: Inference and Visualisation of the
475 Chemoattractant Field Driving Cell Chemotaxis In Vivo. PLoS ONE. 2012 Apr
476 26;7(4):e35182.

477 23. Oehlers SH, Flores MV, Okuda KS, Hall CJ, Crosier KE, Crosier PS. A chemical
478 enterocolitis model in zebrafish larvae that is dependent on microbiota and responsive
479 to pharmacological agents. Dev Dyn. 2011 Jan 1;240(1):288–98.

480 24. Rolig AS, Parthasarathy R, Burns AR, Bohannan BJM, Guillemin K. Individual
481 Members of the Microbiota Disproportionately Modulate Host Innate Immune
482 Responses. Cell Host Microbe. 2015 Nov 11;18(5):613–20.

483 25. Bates JM, Akerlund J, Mittge E, Guillemin K. Intestinal alkaline phosphatase detoxifies
484 lipopolysaccharide and prevents inflammation in zebrafish in response to the gut
485 microbiota. Cell Host Microbe. 2007 Dec 13;2(6):371–82.

486 26. Kanther M, Tomkovich S, Xiaolun S, Grosser MR, Koo J, Flynn EJ, et al. Commensal
487 microbiota stimulate systemic neutrophil migration through induction of serum
488 amyloid A. Cell Microbiol. 2014 Jul;16(7):1053–67.

489 27. Renshaw SA, Loynes CA, Trushell DMI, Elworthy S, Ingham PW, Whyte MKB. A
490 transgenic zebrafish model of neutrophilic inflammation. Blood. 2006 Dec
491 15;108(13):3976–8.

492 28. Bates JM, Mittge E, Kuhlman J, Baden KN, Cheesman SE, Guillemin K. Distinct signals
493 from the microbiota promote different aspects of zebrafish gut differentiation. Dev
494 Biol. 2006;297(2):374–86.

495 29. Spomer W, Pfriem A, Alshut R, Just S, Pylatiuk C. High-throughput screening of
496 zebrafish embryos using automated heart detection and imaging. J Lab Autom. 2012
497 Dec;17(6):435–42.

498 30. Letamendia A, Quevedo C, Ibarbia I, Virto JM, Holgado O, Diez M, et al. Development
499 and Validation of an Automated High-Throughput System for Zebrafish In Vivo
500 Screenings. PLOS ONE. 2012 May 15;7(5):e36690.

501 31. Liu X, Painter RE, Enesa K, Holmes D, Whyte G, Garlisi CG, et al. High-throughput
502 screening of antibiotic-resistant bacteria in picodroplets. Lab Chip. 2016 Apr
503 26;16(9):1636–43.

504 32. Westhoff JH, Giselbrecht S, Schmidts M, Schindler S, Beales PL, Tönshoff B, et al.
505 Development of an Automated Imaging Pipeline for the Analysis of the Zebrafish
506 Larval Kidney. PLOS ONE. 2013 Dec 4;8(12):e82137.

507 33. ImageXpress Micro XLS Widefield High-Content Analysis System | Molecular Devices.
508 Available from: https://www.moleculardevices.com/products/additional-
509 products/imagexpress-micro-xls-widefield-high-content-analysis-system#gref

510 34. ACQUIFER. Screening. ACQUIFER. Available from:
511 https://www.acquifer.de/screening/

512 35. Biometrica S 180 Blackfly Interactive, Union. Union Biometrica | VAST BioImager™
513 Platform Overview. 2010. Available from: http://www.unionbio.com/vast/

514 36. Jemielita M, Taormina MJ, Delaurier A, Kimmel CB, Parthasarathy R. Comparing
515 phototoxicity during the development of a zebrafish craniofacial bone using confocal
516 and light sheet fluorescence microscopy techniques. J Biophotonics. 2013;6:920–8.

517 37. Dunsby C. Optically sectioned imaging by oblique plane microscopy. Opt Express. 2008
518 Dec 8;16(25):20306–16.

519 38. Bouchard MB, Voleti V, Mendes CS, Lacefield C, Grueber WB, Mann RS, et al. Swept
520 confocally-aligned planar excitation (SCAPE) microscopy for high-speed volumetric
521 imaging of behaving organisms. Nat Photonics. 2015 Feb;9(2):113–9.

522 39. Westerfield M. The zebrafish book. A guide for the laboratory use of zebrafish (Danio
523 rerio). Vol. 5th. Eugene, OR: University of Oregon Press; 2007. Available from:
524 http://zfin.org/zf_info/zfbook/zfbk.html

525 40. Gonzalez RC, Woods RE. Digital Image Processing. Upper Saddle River, N.J.: Prentice
526 Hall; 2008.

527

528

529

530 **SUPPORTING INFORMATION CAPTIONS:**

531

532 **Supplemental Movie 1.** Video of the automated, high-throughput light sheet microscope in
533 operation. After a larval zebrafish, flowing through tubing, is detected and positioned, 3D
534 scans in two colors in two different regions, are obtained. The final image (0:57-1:03) is of
535 tdTomato-labeled bacteria and GFP-labeled neutrophils.

536

537 **Supplemental Movie 2.** A light sheet fluorescence scan through the anterior intestine of a
538 larval zebrafish with GFP-expressing neutrophils evident as very bright objects above
539 autofluorescent background. The total image depth is 475 μm (2.5 μm/slice x 190 slices).
540 The maximum intensity projection of this scan is shown in Figure 2E.

541

542 **Supplemental Figure 1.** Sample brightfield images of four larval zebrafish, captured and
543 saved prior to light sheet fluorescence imaging. Notably, the orientation is random in the
544 capillary, with a tendancy toward either "gut down" or "gut up." Scale bar: 100 μm.

545

546 **Supplemental Figure 2.** The number of neutrophils in 67 larval zebrafish, assessed from
547 two-dimensional maximum intensity projections and from the full three-dimensional light
548 sheet fluorescence scans. The former is 0.76 ± 0.02 of the latter, indicating that three-
549 dimensional imaging is necessary to capture all the cells in a three-dimensional volume.

550